Electronic Supplementary Material (ESI) for Journal of Materials Chemistry A.
This journal is © The Royal Society of Chemistry 2023

Supplementary Information

Zinc Porphyrin-Based Halogen-bonded Organic Framework with Heavy Atoms as Highly Efficient Photocatalyst for Oxidative Coupling of Amines

Penghao Sun, Hongqiang Dong, Siheng Lv, Yongfei Yin, Guanfei Gong, Lu Wang, Jike Wang and Shigui Chen*

The Institute for Advanced Studies, Wuhan University, 299 Bayi Road, Wuhan, Hubei 430072 China

Table of Content

Materials and Methods **5**

Materials and Characterization 5

Electrochemical measurements 5

Computational methods 5

Photocatalytic Reaction 5

Synthesis **6**

Synthesis of **H_2TPP** 6

Synthesis of **ZnTPP** 6

Synthesis of **XOF-ZnTPP** 6

Results and Discussion **7**

Figure S1. XPS spectra of **XOF-ZnTPP**. 7

Figure S2. Partial ^{1}H NMR spectra of **ZnTPP** and **XOF-ZnTPP**. 7

Figure S3. ATR-FTIR spectra of **H_2TPP**, **ZnTPP**, and **XOF-ZnTPP**. 7

Figure S4. UV-vis spectra of **ZnTPP** and **XOF-ZnTPP**. 8

Figure S5. Digital photographs of **ZnTPP** and **XOF-ZnTPP**. 8

Figure S6. The XRD patterns of **XOF-ZnTPP** after treatment in different solvents. 8

Figure S7. TGA curve of **ZnTPP** and **XOF-ZnTPP**. 9

Figure S8. N_2 sorption isotherms plots of **XOF-ZnTPP**. 9

Figure S9. Comparison of experimental and simulated PXRD patterns of different models. 10

Figure S10. Side view of different **XOF-ZnTPP** models. 10

Figure S11. TEM picture **XOF-ZnTPP**. 10

Figure S12. Tauc plots of **ZnTPP** and **XOF-ZnTPP**. 11

Figure S13. Mott-Schottky plots of **XOF-ZnTPP** 11

Figure S14. The UV-vis absorption of ABDA with **XOF-ZnTPP** and **ZnTPP.** 12

Figure S15. The UV-vis absorption of NBT with **XOF-ZnTPP** and **ZnTPP** 13

Figure S16. Comparison of the decay rate of NBT 13

Figure S17. EPR detection of $O_2^{\bullet-}$ trapped by TEMP in MeOH 14

Figure S18. The flourescence of TAOH at different irradiation time (blue LED, 50 W). 14

Figure S19. The fluorescence change rate of TAOH 14

Figure S20. EPR detection of •OH trapped by DMPO in H_2O 15

Figure S21. The optimized structures of **ZnTPP** and **$[(ZnTPP)_2I]^+$**. 15

Table S1. The excitation energies of **ZnTPP** and **$[(ZnTPP)_2I]^+$**. 15

Figure S22. The energy gap between S1, S2 and its nearest triplet excited state. 15

Table S2. Selective aerobic oxidation of benzylamine under different conditions. 16

Figure S23. ^{1}H NMR spectra of the benzylamine coupling reaction under different LED light. 16

Figure S24. Wavelength-dependent reaction yields of **XOF-ZnTPP**. 17

Figure S25. Quenching experiments of ROS for oxidation of benzylamine. 17

Figure S26. PXRD and FTIR spectra of **XOF-ZnTPP** before and after photocatalysis. 17

Figure S27. TEM of **XOF-ZnTPP** before and after photocatalysis, respectively. 18

Figure S28. Assessment of catalytic stability of **XOF-ZnTPP**. 18

^{1}H NMR spectra 19

Figure S29. ^{1}H NMR spectra of **H_2TPP**. 19

Figure S30. ^{1}H NMR spectra of **ZnTPP**. 19

Figure S31. ^{1}H NMR spectra of N-benzylidenebenzylamine. 20

Figure S32. ^{1}H NMR spectra of N-(2-methylbenzylidene)-2-methylphenylmethylamine. 20

Figure S33. ^{1}H NMR spectra of N-(3-methylbenzylidene)-3-methylphenylmethylamine. 21

Figure S34. ^{1}H NMR spectra of N-(4-methylbenzylidene)-4-methylphenylmethylamine 21

Figure S35. ^{1}H NMR spectra of N-(4-methoxybenzylidene)-4-methoxybenzylamine. 22

Figure S36. ^{1}H NMR spectra of N-[4-(trifluoromethyl)benzyl]-1-[4-(trifluoromethyl)phenyl]methanimine. 22

Figure S37. ^{1}H NMR spectra of N-(4-bromobenzyl)-1-(4-bromophenyl) methanimine. 23

Figure S38. ^{1}H NMR spectra of N-(4-methoxycarbonylbenzyl)-N-(4-methoxycarbonylbenzylidene) amine. 23

Figure S39. ^{1}H NMR spectra of (4-(((4-(hydroxymethyl)benzyl)imino)methyl)phenyl)methanol. 24

Figure S40. ^{1}H NMR spectra of N-(2-thienylmethylidene)-2-thienylmethylamine. 24

Materials and Methods

Materials and Characterization

All starting materials and solvents were obtained from commercial suppliers and used without further purification. Analytical thin-layer chromatography (TLC) was performed on silica-gel plate w/UV254 (200 μm). The ^{1}H NMR spectra were recorded on 400 MHz spectrometer (Bruker AVANCE NEO 600 spectrometer) in the indicated solvents. Chemical shifts are expressed in parts per million (δ) using residual solvent protons as internal standard. The couple constants values (J) are in Hertz (Hz). The following abbreviations were used for signal multiplicities: s, singlet; d, doublet. Solid-state diffuse reflectance UV-vis spectra characterized by Lambda 750S. Powder XRD patterns were recorded on Rigaku SmartLab SE diffractometer (CuKα, λ = 1.5405 Å, 45 kV, 200 mA). Scanning electron microscopy (SEM) images were recorded on field emission scanning electron microscope (Tescan CLARA). X-ray photoelectron spectroscopy (XPS) was performed in ESCALAB 250Xi (The adventitious carbon located at 284.8 eV was used to calibrate samples without the carbon themselves). The morphologies of materials were characterized using field emission transmission electron microscopy (FE-TEM, F200). ESR spectra were recorded on a Bruke A200 spectrophotometer at 298 K.

Electrochemical measurements

Electrochemical impedance spectroscopy (EIS), transient photocurrent response, and Mott-Schottky plots were performed on a CHI660E electrochemical workstation (Chenhua Instruments Co., Shanghai) with a standard three-electrode system. 0.50 M Na_2SO_4 water solution was used as the electrolyte. Pt film and Ag/AgCl electrode were used as counter electrode and reference electrode, respectively. The working electrodes were prepared as follows: the photocatalyst powder (2 mg) and 5.0 wt% Nafion solution (5 μL) were dispersed in ethanol (0.2 mL). After sonication for 30 min, the obtained ink was uniformly pipetted onto a piece of indium tin oxide (ITO) conductive glass with a deposition area of 1 × 1 cm^2 and dried at 50 °C for 4 hours. The light source used for transient photocurrent response measurements was a 300 W Xe lamp.

Computational methods

All the calculations were performed with density functional theory (DFT)[1] and time-dependent density functional theory (TDDFT)[2] implemented in Gaussian 09 program package[3]. The ground-state geometry optimizations of **ZnTPP** and **[(ZnTPP)$_2$I]$^+$** molecules were performed at B3LYP/3-21G level.[4,5] The excited energy at B3LYP/3-21G TD level was calculated from the optimized ground state structures without further relaxation. The vertical transition energies were obtained by the difference between the energies of the lowest excited state and the ground state.

Photocatalytic Reaction

For photocatalytic oxidative coupling of amines, 0.55 mL of CD_3CN, 0.1 mmol of substrate, and 2 mg of catalysts were added into a 5 mL glass vessel. After ultrasonic treatment of 10 s, the mixture was irradiated with a blue LED (50 W, 460 ~ 465 nm). The reaction was monitored by TLC and the yield was analyzed by ^{1}H NMR without treatment. The catalysts were separated by centrifugation and washed by DCM and MeOH for recycling.

Synthesis

Synthesis of 5,10,15,20-tetrakis(4-pyridyl) porphyrin (H_2TPP)[6]

4-Pyridine carboxaldehyde (8.8 mL, 93.4 mmol) was added to propionic acid (700 mL), then pyrrole (6.5 mL, 93.4 mmol) was added under stirring. The mixture was refluxed overnight. After cooled to room temperature, the solvent was evaporated under reduced pressure, and the resulting solid was washed by DMF (2×100 mL) and hot MeOH (2×250 mL). The filtrate was dried under vacuum to obtain pure **H_2TPP** (dark purple powder, 4.05 g, 28%). ^{1}H NMR (600 MHz, 298K, DMSO-d_6, ppm): δ 9.06 (dd, J_1 = 5.8 Hz, J_2 = 2.5 Hz, 8H); 8.92 (s, 8H), 8.28 (dd, J_1 = 5.8 Hz, J_2 = 2.5 Hz, 8H); -3.06 (s, 2H).

Synthesis of 5,10,15,20-tetrakis(4-pyridyl) zinc(II) porphyrin (ZnTPP)[6]

Pure H_2TPP (1.0 g, 1.6 mmol) was dissolved in a mixture of chloroform (20 mL) and methanol (5 mL) with zinc acetate (1.2 g, 6.5 mmol). The mixture was refluxed under stirring for 8 h. After cooled to room temperature, the solvent was evaporated under reduced pressure, and the resulting solid was washed with hot MeOH (2×250 mL) and water (100 mL). The filtrate was dried under vacuum to obtain pure **ZnTPP** (violet powder, 1.1 g, 99%). ^{1}H NMR (600 MHz, 298K, DMSO-d_6, ppm): δ 9.02 (dd, J_1 = 5.8 Hz, J_2 = 2.5 Hz, 8H); 8.84 (s, 8H), 8.22 (dd, J_1 = 5.8 Hz, J_2=2.5 Hz, 8H).

Synthesis of XOF-ZnTPP

$AgBF_4$ (23 mg, 0.11 mmol) in methanol (5 mL) was added dropwise into a solution of **ZnTPP** (40 mg, 0.05 mmol) in $CHCl_3$/MeOH (30 mL, v/v = 1:4) mixed solution. After the solution was stirred for 1 hour at room temperature, a methanol solution of iodine (30 mg, 0.11 mmol) was added by drops. and the mixture was stirred for another 1 hour at room temperature. Then, the solvent was removed by filtrating. The residue solid was dried under vacuum to obtain **XOF-ZnTPP** (black solid, 80 mg, 68%). ^{1}H NMR (600 MHz, 298K, DMSO-d_6, ppm): 9.05 (d, J = 5.8 Hz 8H); 8.86 (s, 8H), 8.27 (d, J = 5.8 Hz 8H). The synthesized material was further annealed in DMSO at 120 °C for 2 hours to obtain crystallized **XOF-ZnTPP**.

Results and Discussion

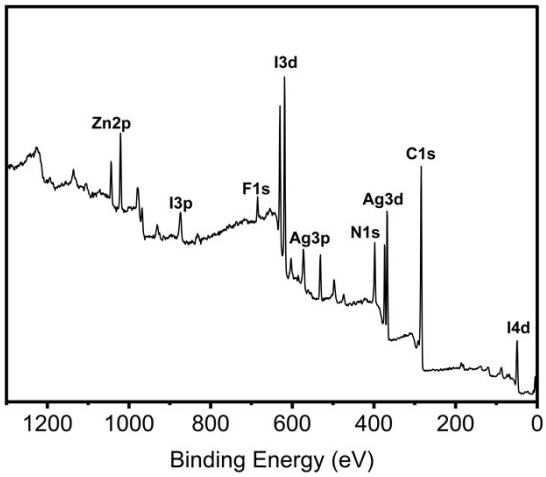

Figure S1. XPS spectra of **XOF-ZnTPP**.

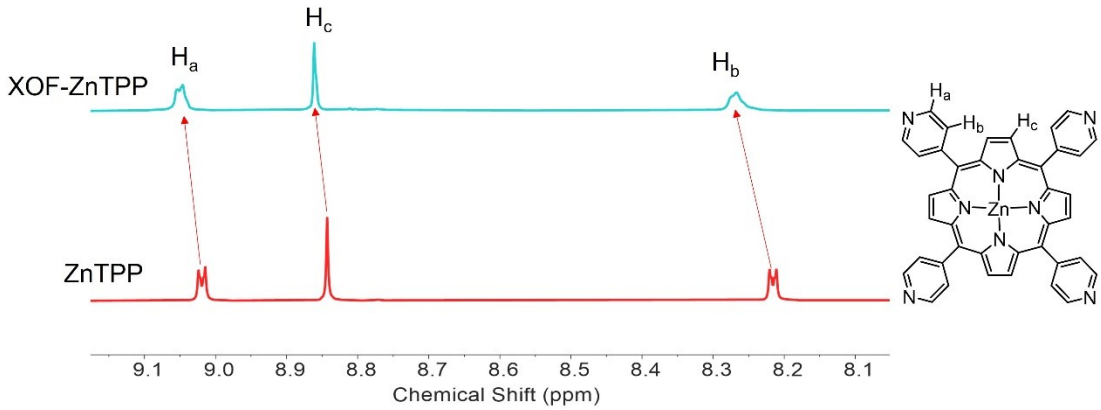

Figure S2. Partial ^{1}H NMR spectra of **ZnTPP** and **XOF-ZnTPP** (DMSO-d_6, 600 MHz, 298 K).

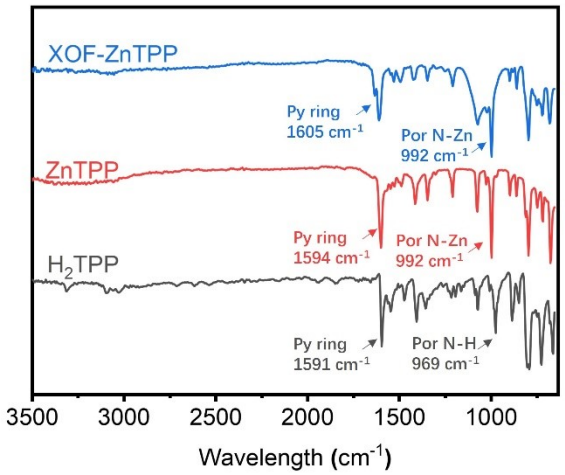

Figure S3. ATR-FTIR spectra of **H_2TPP**, **ZnTPP**, and **XOF-ZnTPP**.

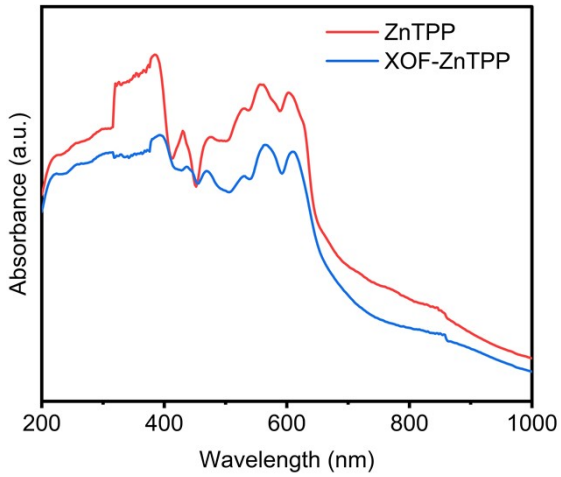

Figure S4. Solid-state diffuse reflectance UV-vis spectra of **ZnTPP** and **XOF-ZnTPP**.

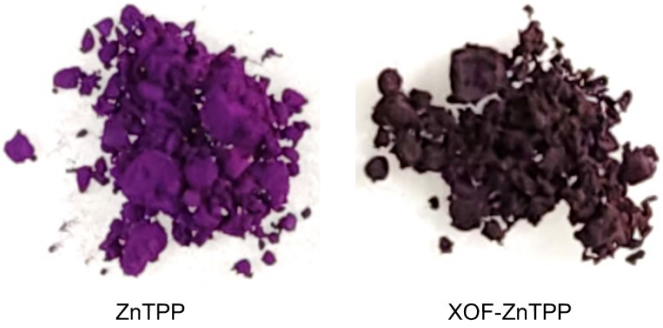

Figure S5. Digital photographs of **ZnTPP** and **XOF-ZnTPP**.

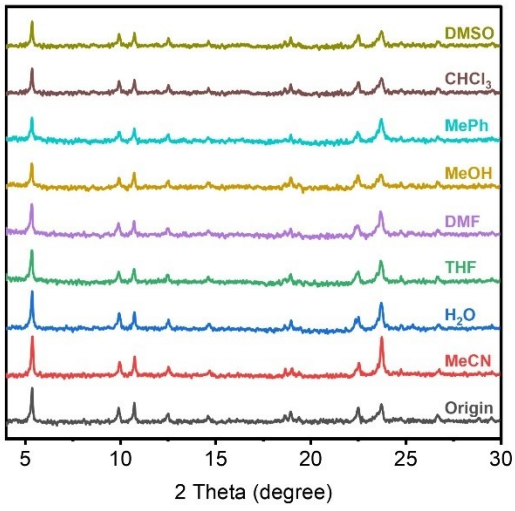

Figure S6. The PXRD patterns of **XOF-ZnTPP** after treatment in different solvents at room temperature for 24 hours.

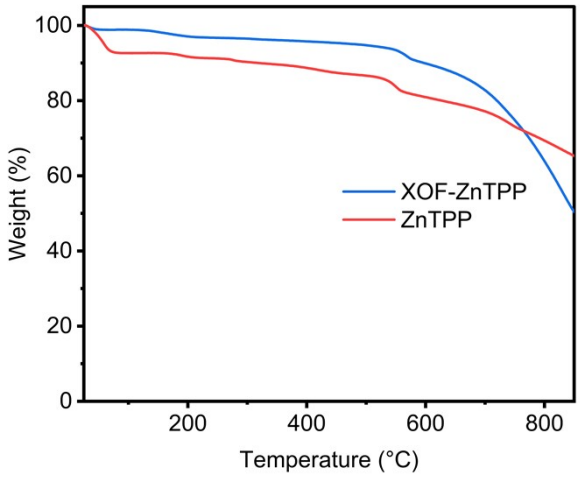

Figure S7. TGA curve of **ZnTPP** and **XOF-ZnTPP**.

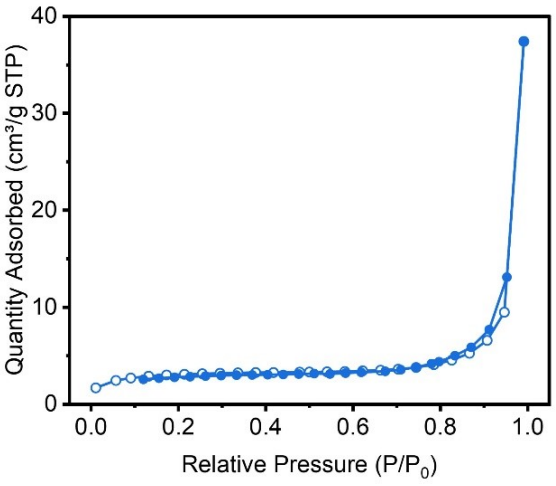

Figure S8. N_2 sorption isotherms plots of **XOF-ZnTPP**.

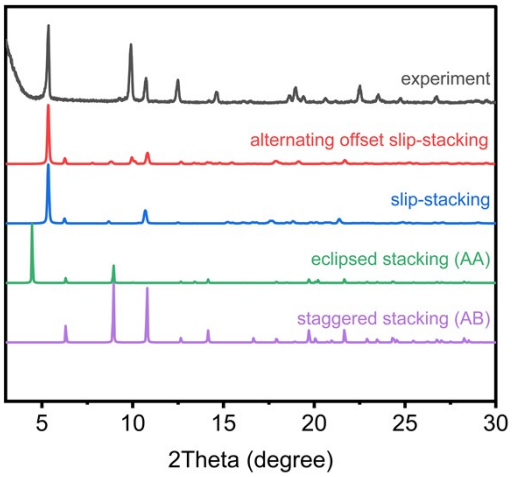

Figure S9. Comparison of experimental and simulated PXRD patterns of different models.

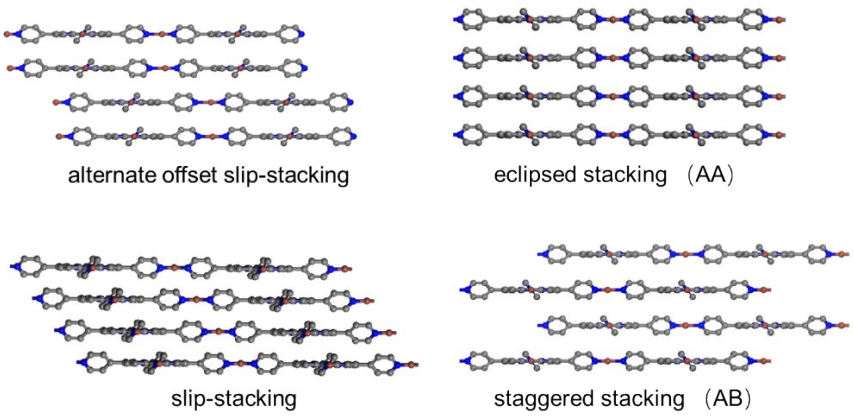

Figure S10. Side view of different **XOF-ZnTPP** models.

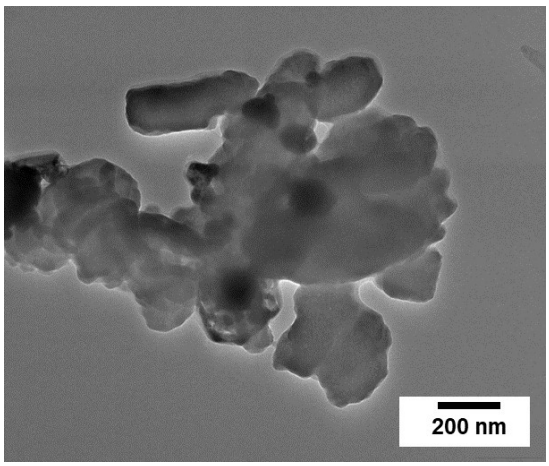

Figure S11. TEM picture **XOF-ZnTPP**.

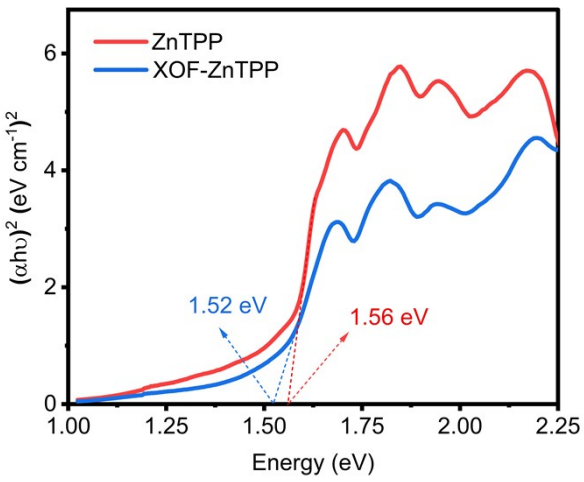

Figure S12. Tauc plots of **ZnTPP** and **XOF-ZnTPP**.

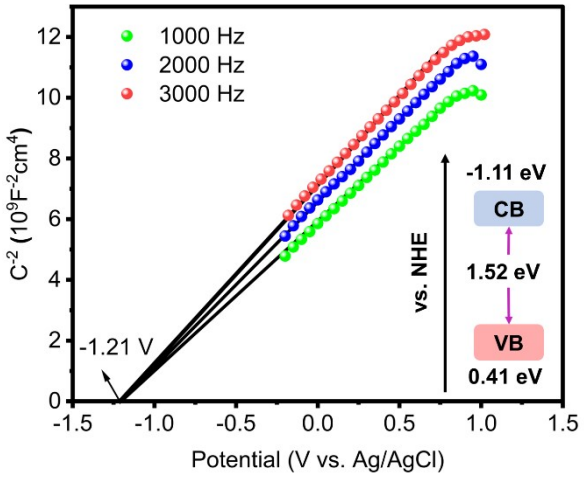

Figure S13. Mott-Schottky plots of **XOF-ZnTPP** (insert: conduction band and valence band potentials of the **XOF-ZnTPP**).

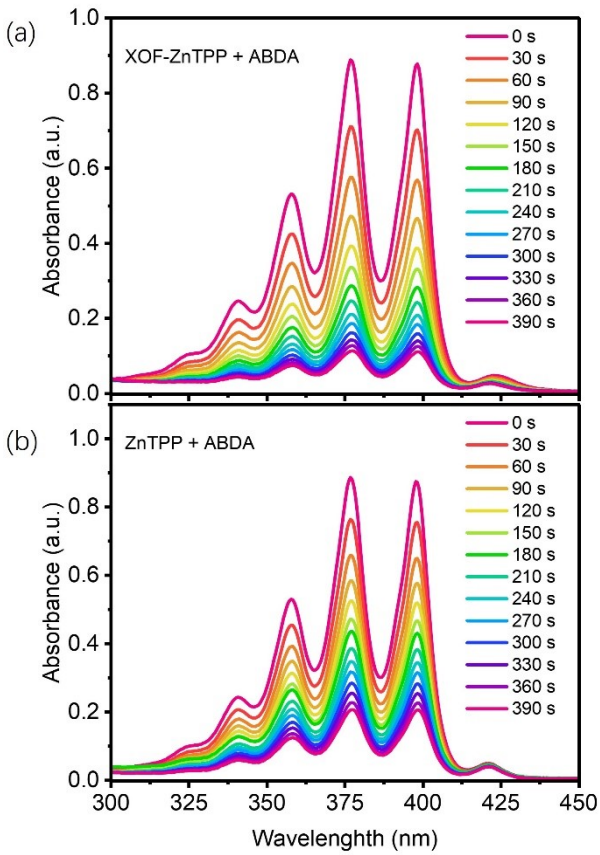

Figure S14. The UV-vis absorption of ABDA with (a) **XOF-ZnTPP** and (b) **ZnTPP** at different irradiation time (blue LED, 50 W).

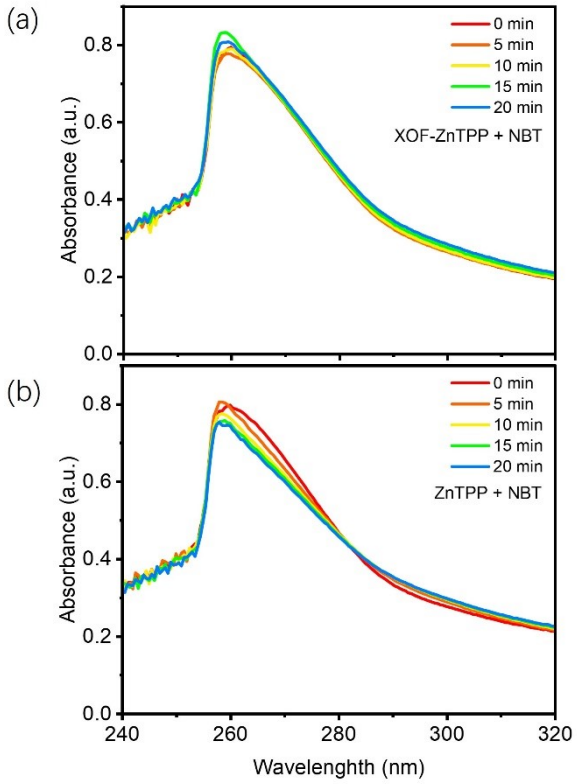

Figure S15. The UV-vis absorption of NBT with (a) **XOF-ZnTPP** and (b) **ZnTPP** at different irradiation time (blue LED, 50 W).

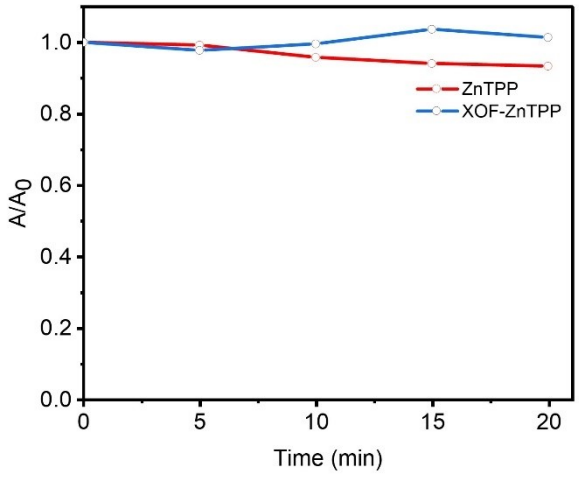

Figure S16. Comparison of the decay rate of NBT with **ZnTPP** and **XOF-ZnTPP** under different irradiation time.

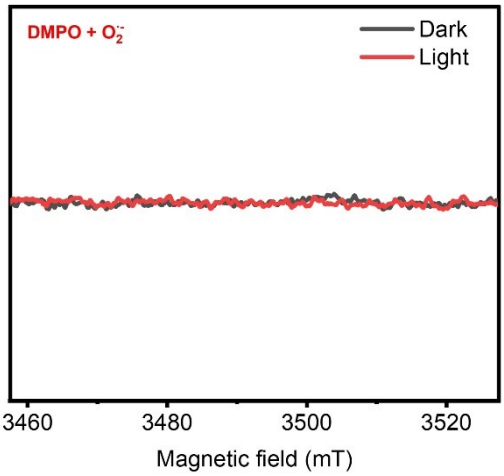

Figure S17. EPR detection of $O_2^{\bullet-}$ trapped by TEMP in MeOH

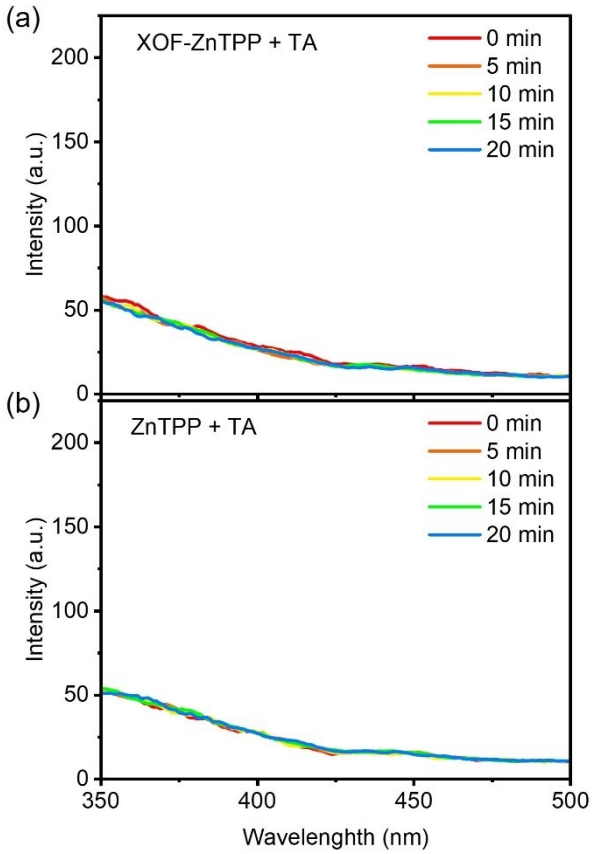

Figure S18. The fluorescence of TAOH (E_x = 310 nm, E_m = 420 nm) with (a) **XOF-ZnTPP** and (b) **ZnTPP** at different irradiation time (blue LED, 50 W). TA can react with •OH to generate 2-hydroxyterephthalic acid (TAOH), which has specific fluorescence emission at 420nm.

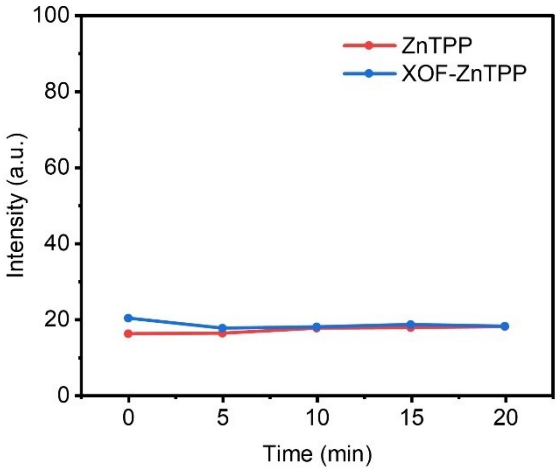

Figure S19. Comparison of the fluorescence change rate at 420 nm of TAOH with **ZnTPP** and **XOF-ZnTPP** under different irradiation time.

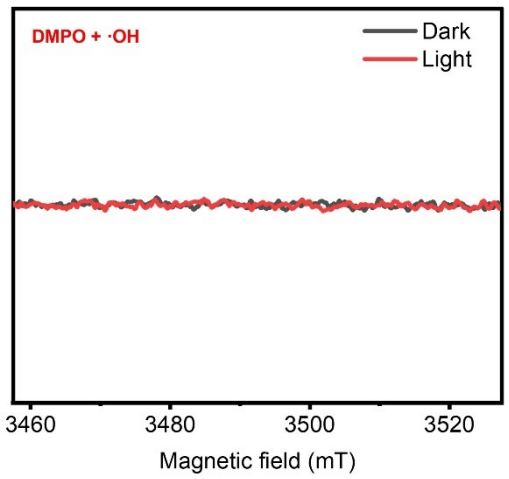

Figure S20. EPR detection of •OH trapped by DMPO in H_2O

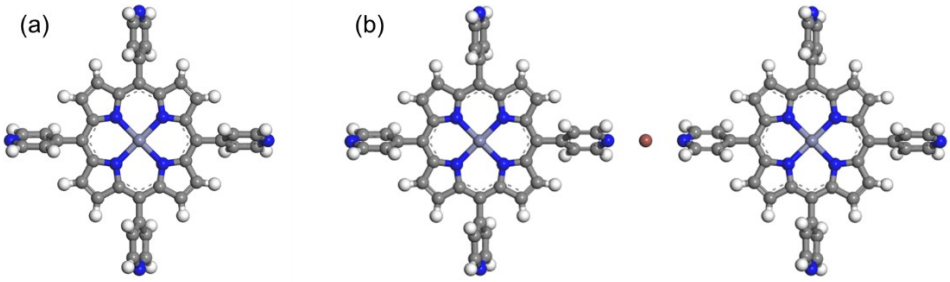

Figure S21. The optimized structures of **ZnTPP** and **[(ZnTPP)$_2$I]$^+$**.

Table S1. The excitation energies of the first 9 singlet and triplet excited states for model molecules **ZnTPP** and **[(ZnTPP)$_2$I]$^+$**.

ZnTPP				$[(ZnTPP)_2I]^+$			
Singlet	Energy (eV)	Triplet	Energy (eV)	Singlet	Energy (eV)	Triplet	Energy (eV)
S1	2.1917	T1	1.8198	S1	1.9655	T1	1.6926
S2	2.1929	T2	1.8201	S2	1.9679	T2	1.6929
S3	2.4577	T3	2.0978(0)	S3	2.2135	T3	1.7802(8)
S4	2.4578	T4	2.0978(4)	S4	2.2136	T4	1.7803(3)
S5	3.4543	T5	2.1427	S5	2.2706	T5	1.9482
S6	3.4546	T6	2.1428	S6	2.2911	T6	1.9483
S7	3.5479	T7	3.0772	S7	2.2917	T7	2.0036(5)
S8	3.5985	T8	3.1335	S8	2.3047	T8	2.0037(2)
S9	3.7251	T9	3.1853	S9	2.4235	T9	2.1230

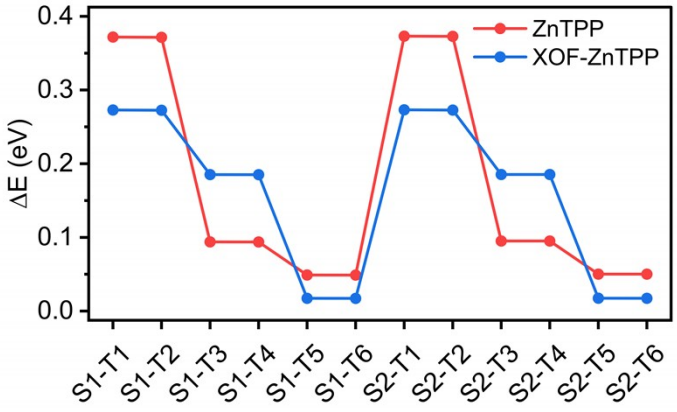

Figure S22. The energy gap between S1, S2 and its nearest triplet excited state.

Table S2. Selective photocatalytic aerobic oxidation of benzylamine under different conditions (0.10mmol benzylamine, 2mg catalyst, 0.55mL solvent, 50W LED).

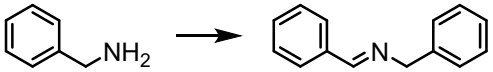

catalyst	light	solvent	time	yield (%)
ZnTPP-XOF	green	CD_3OD	1	51
ZnTPP-XOF	green	CD_3OD	4	96
ZnTPP-XOF	blue	CD_3OD	1	72
ZnTPP-XOF	blue	CD_3OD	2	92
ZnTPP-XOF	green	CD_3CN	1	94
ZnTPP-XOF	blue	CD_3CN	1	98
ZnTPP-XOF	dark	CD_3CN	1	n.d.
ZnTPP	blue	CD_3CN	1	66
AgI	blue	CD_3CN	1	n.d.
/	blue	CD_3CN	1	n.d.

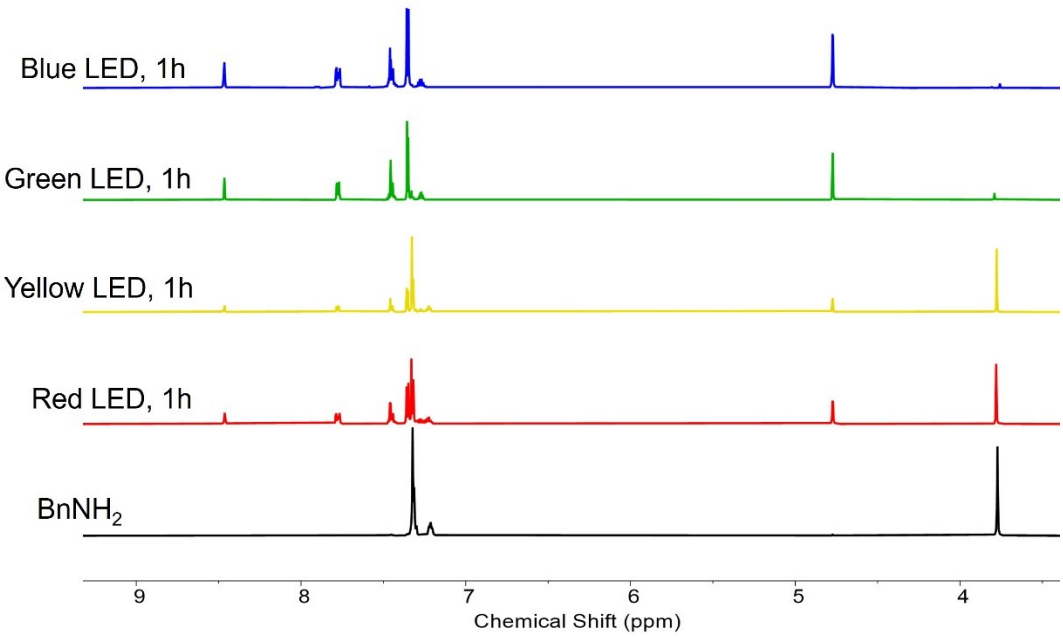

Figure S23. ^{1}H NMR spectra of the benzylamine oxidation coupling reaction catalyzed by **XOF-ZnTPP** under different LEDs light in 1 hour (blue: 460-465 nm, green: 520-525 nm, yellow: 585-590 nm, and red: 620-625 nm, all the LEDs are 50W).

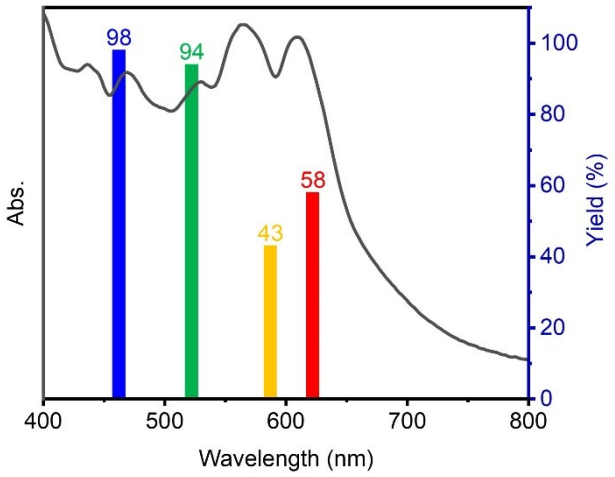

Figure S24. Wavelength-dependent benzylamine oxidation coupling reaction yields of **XOF-ZnTPP** with the absorption curve.

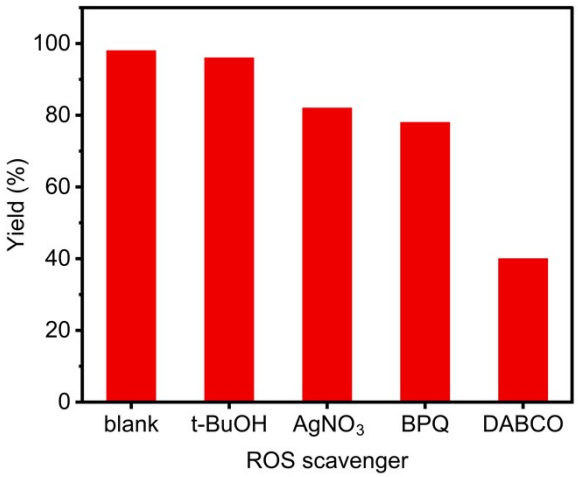

Figure S25. Quenching experiments of ROS for selective aerobic oxidation of benzylamine over **XOF-ZnTPP**.

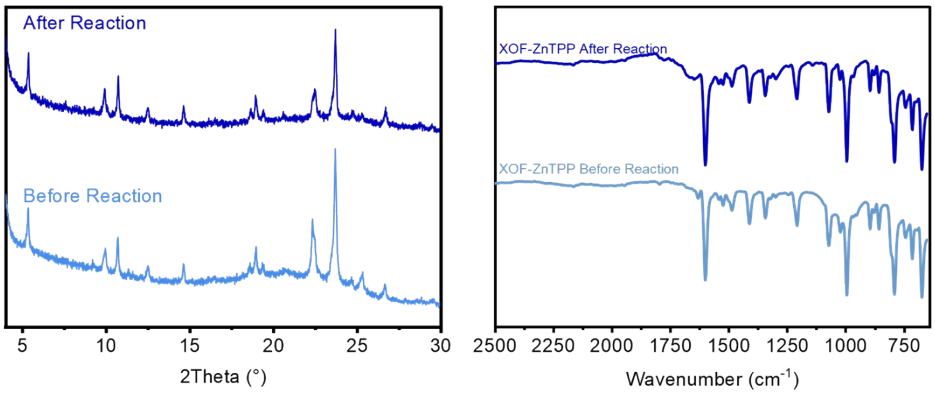

Figure S26. (a) PXRD and (b) ATR-FTIR spectra of **XOF-ZnTPP** before and after

photocatalysis, respectively.

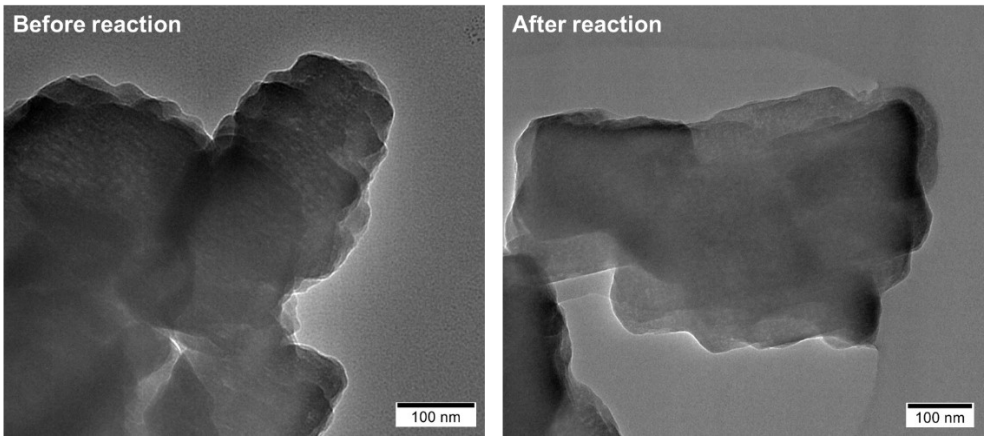

Figure S27. TEM of **XOF-ZnTPP** before and after photocatalysis, respectively.

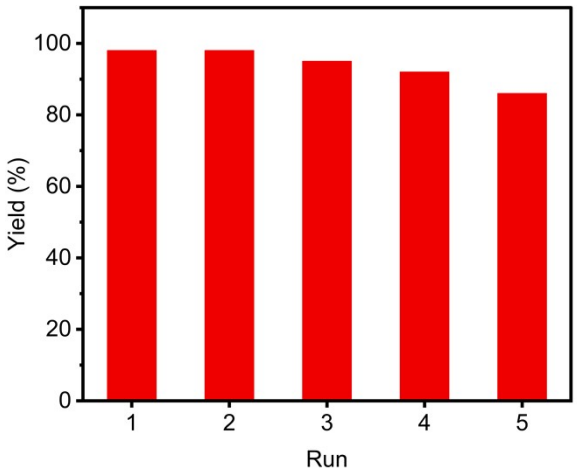

Figure S28. Assessment of catalytic stability of **XOF-ZnTPP**.

^{1}H NMR spectra

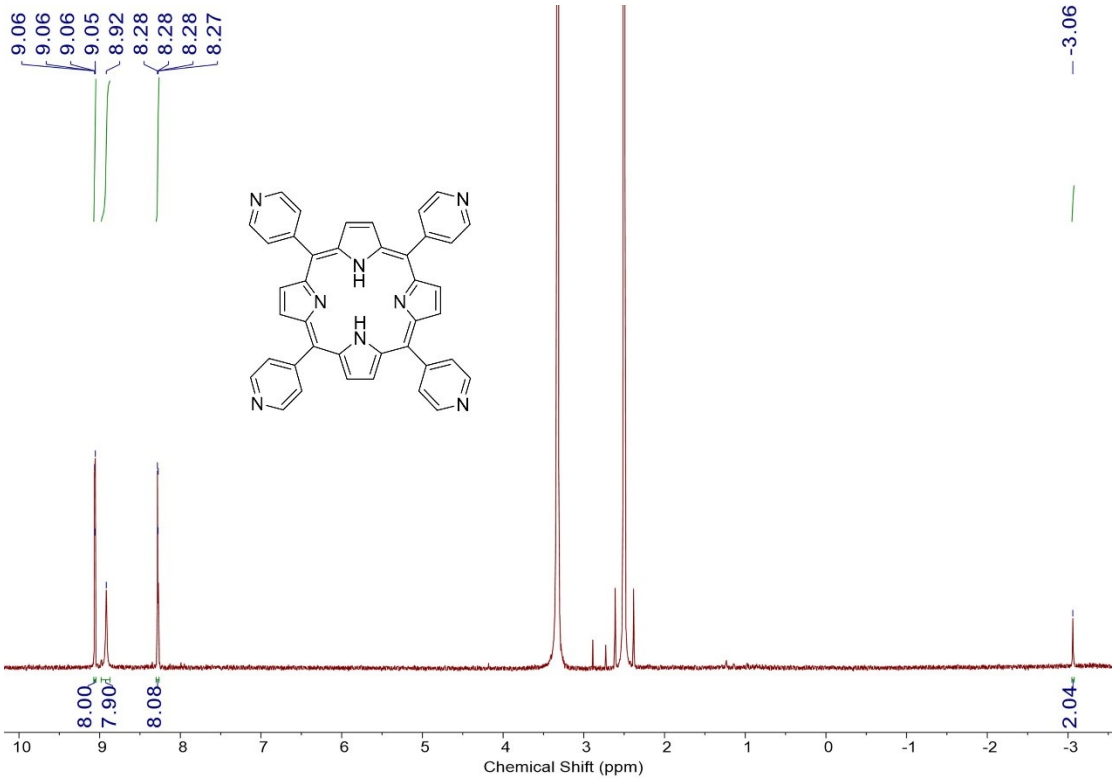

Figure S29. ^{1}H NMR spectra of **H_2TPP** (DMSO-d_6, 600 MHz, 298 K).

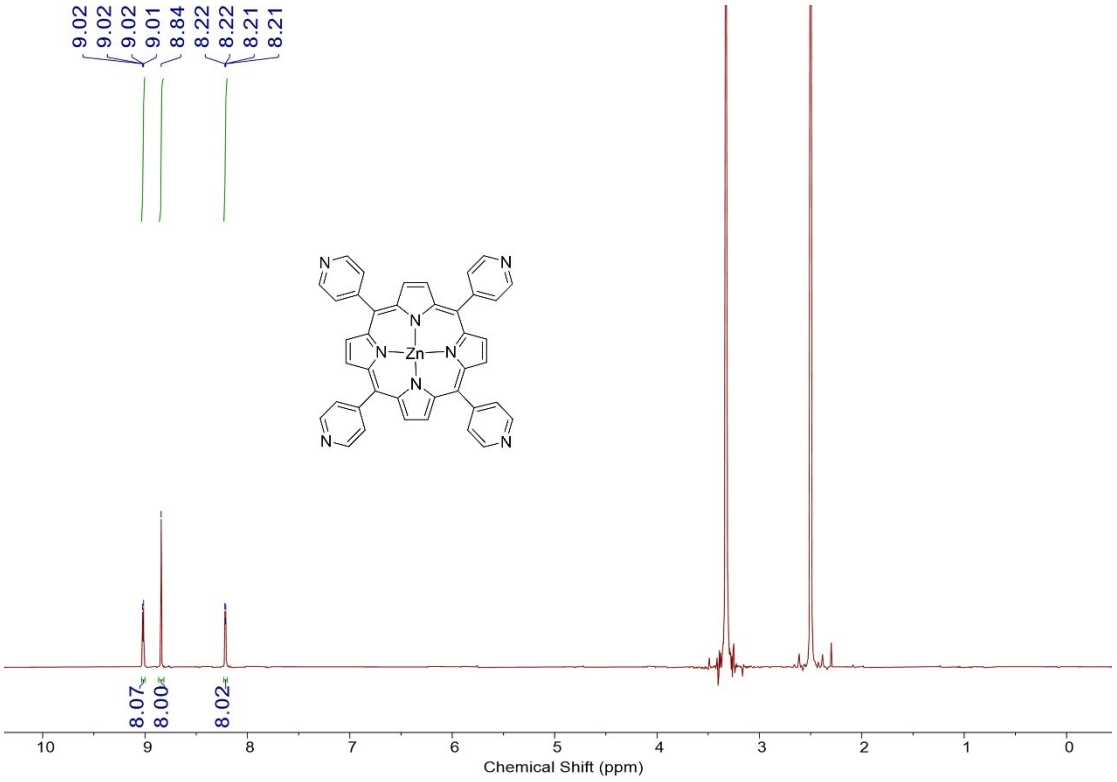

Figure S30. ^{1}H NMR spectra of **ZnTPP** (DMSO-d_6, 600 MHz, 298 K).

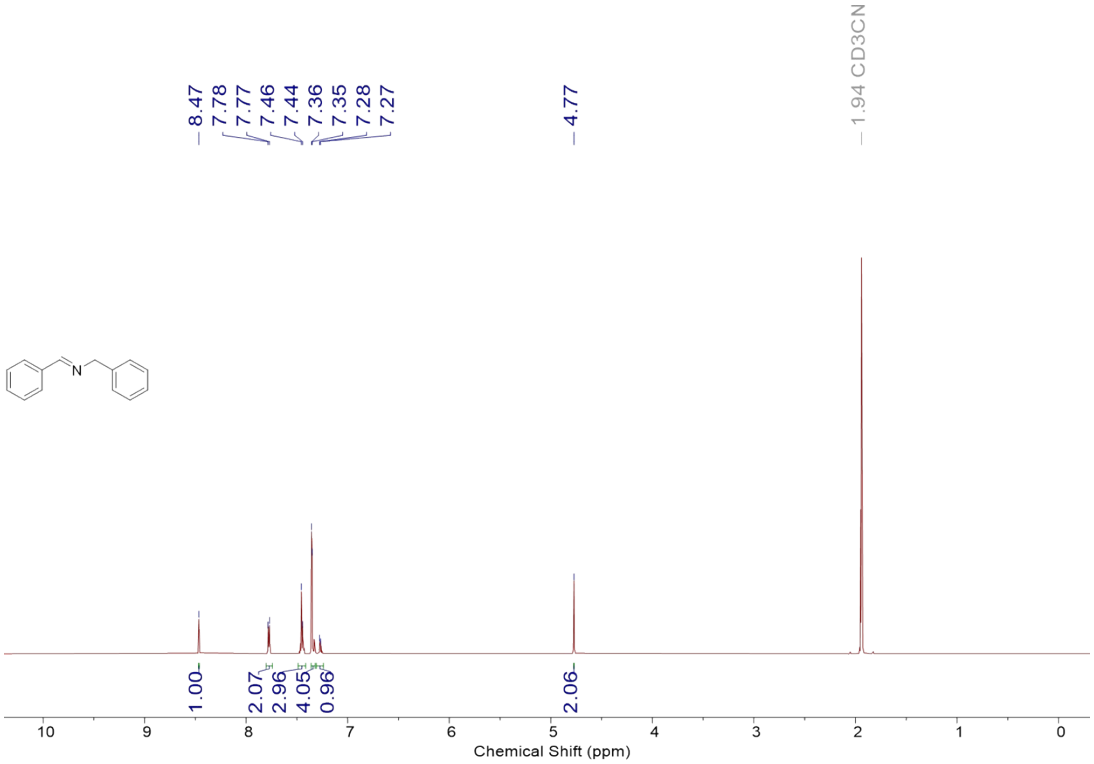

Figure S31. ^{1}H NMR spectra of *N*-benzylidenebenzylamine (CD_3CN, 600 MHz, 298 K).

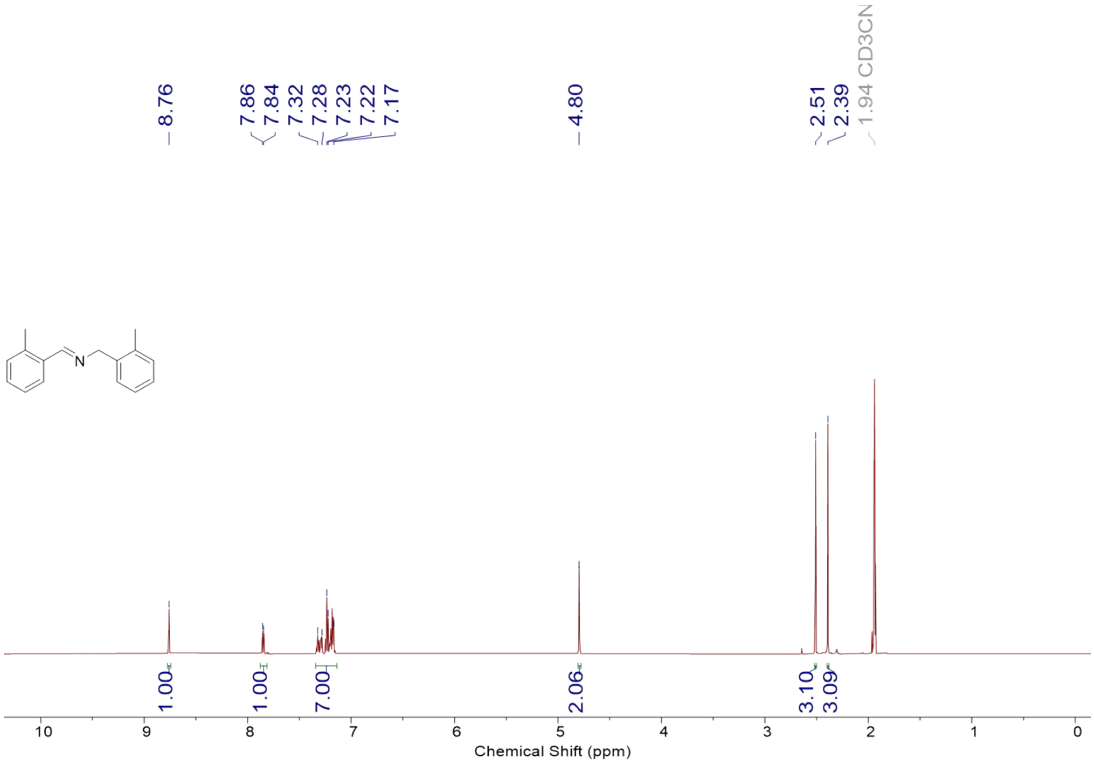

Figure S32. ^{1}H NMR spectra of *N*-(2-methylbenzylidene)-2-methylphenylmethylamine (CD_3CN, 600 MHz, 298 K).

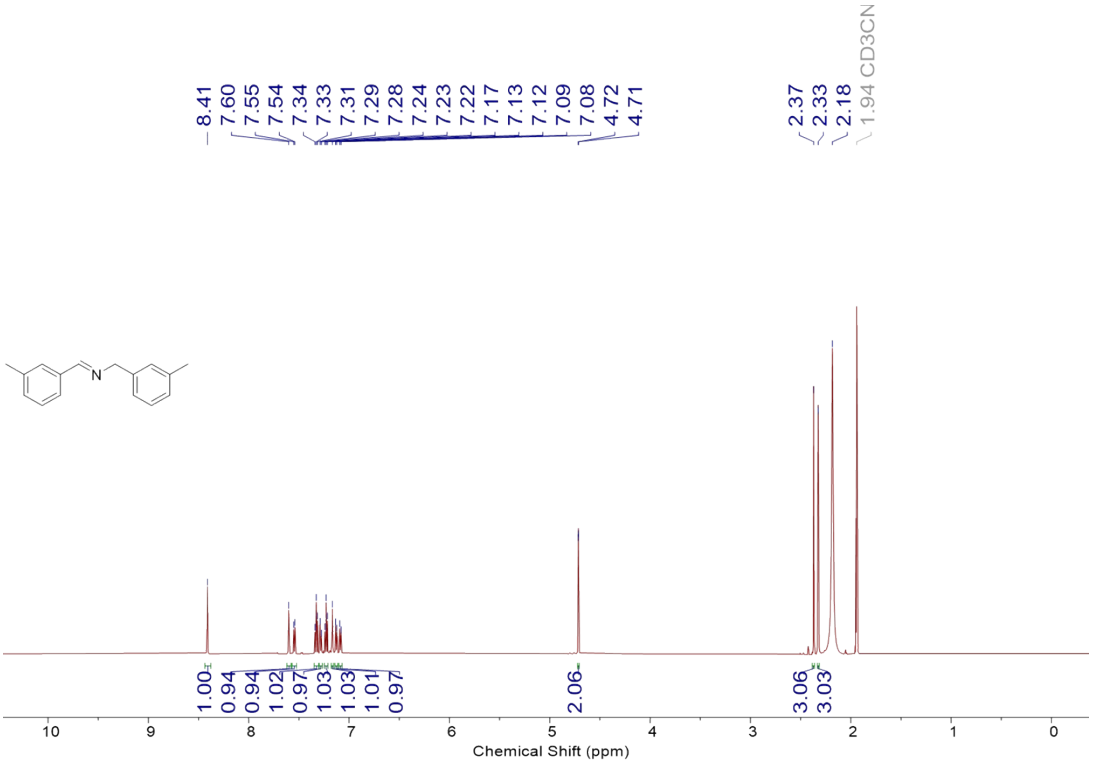

Figure S33. ^{1}H NMR spectra of *N*-(3-methylbenzylidene)-3-methylphenylmethylamine (CD_3CN, 600 MHz, 298 K).

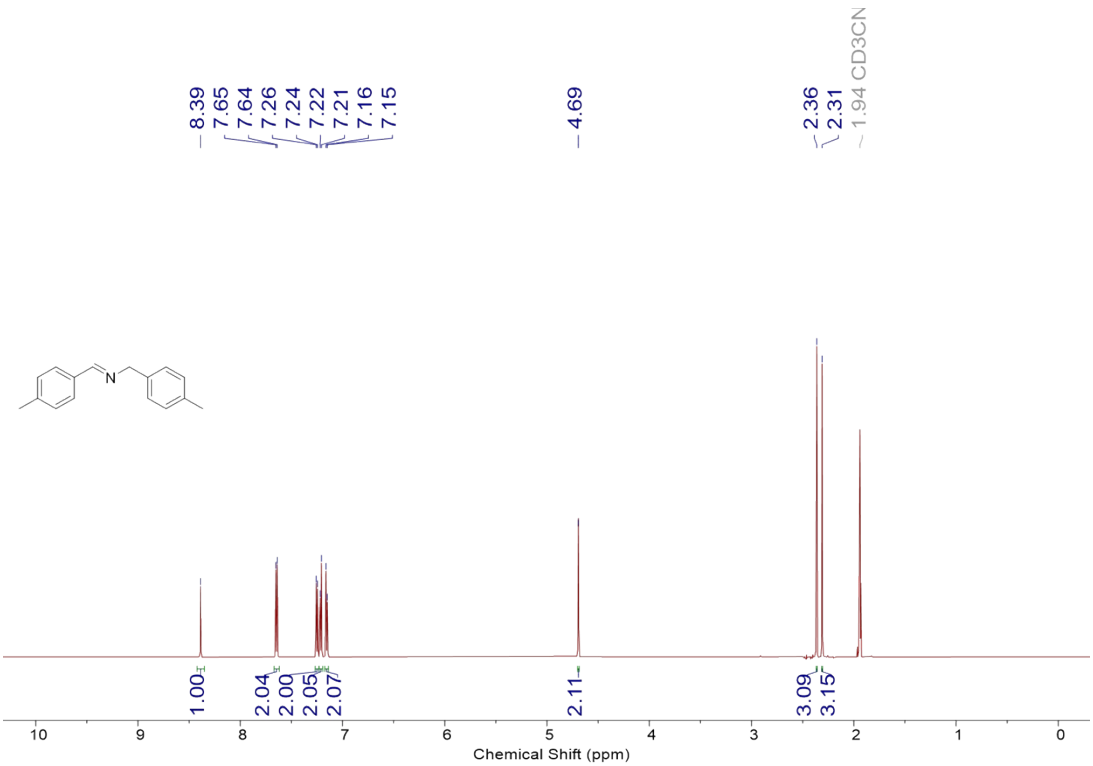

Figure S34. ^{1}H NMR spectra of *N*-(4-methylbenzylidene)-4-methylphenylmethylamine (CD_3CN,

600 MHz, 298 K).

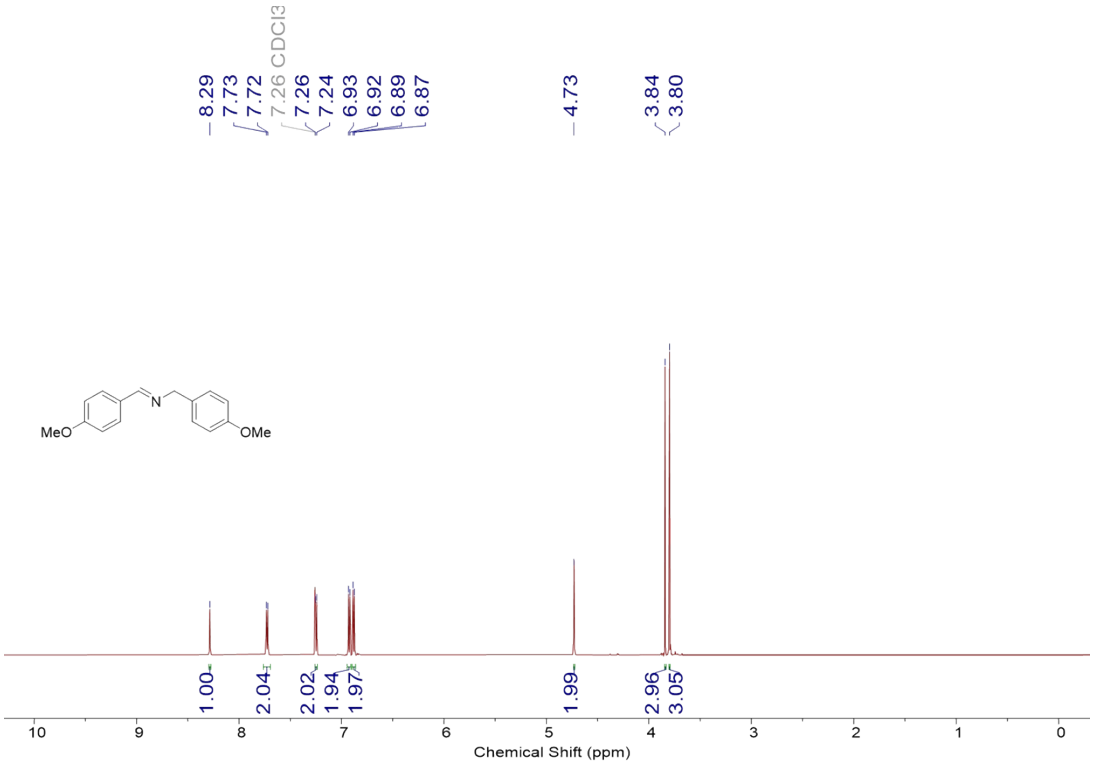

Figure S35. ^{1}H NMR spectra of *N*-(4-methoxybenzylidene)-4-methoxybenzylamine ($CDCl_3$, 600 MHz, 298 K).

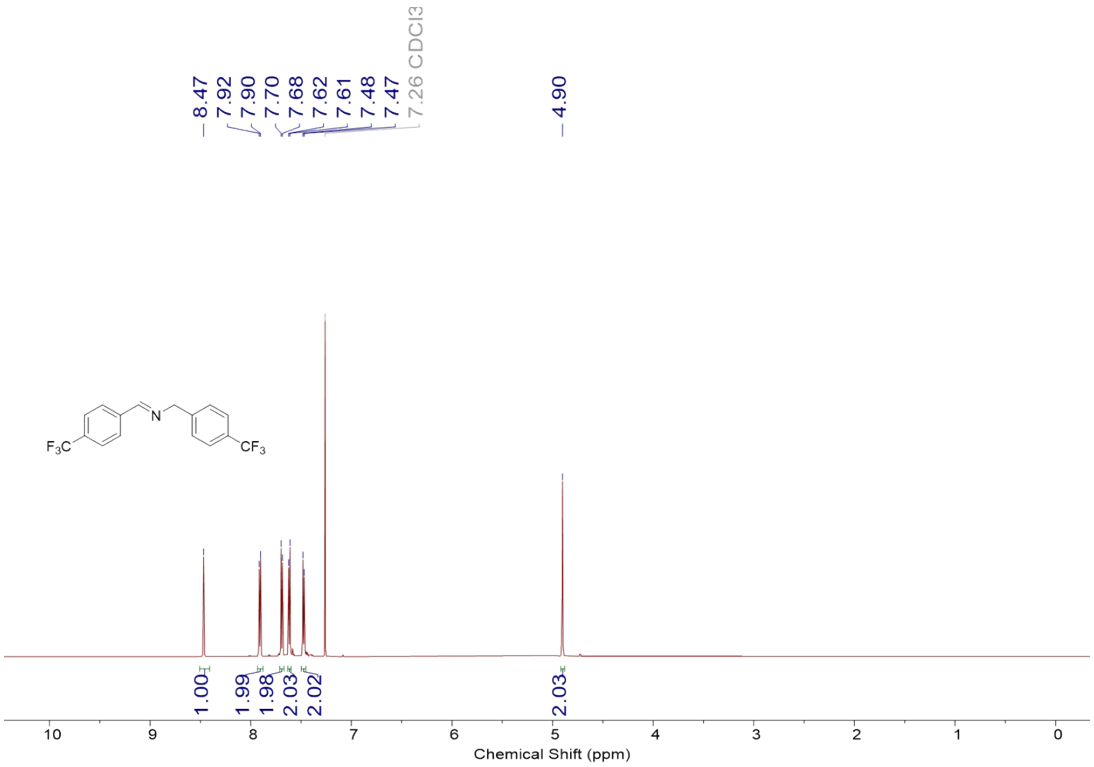

Figure S36. ^{1}H NMR spectra of *N*-[4-(trifluoromethyl)benzyl]-1-[4-(trifluoromethyl)phenyl]methanimine ($CDCl_3$, 600 MHz, 298 K).

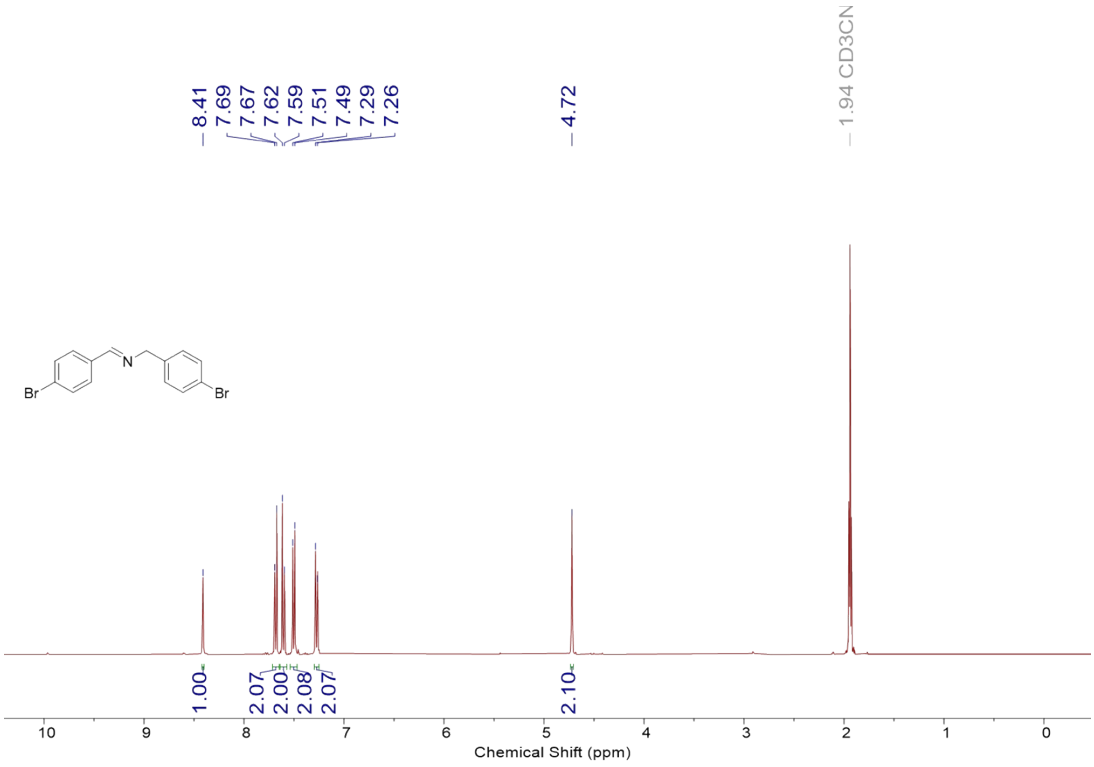

Figure S37. ^{1}H NMR spectra of *N*-(4-bromobenzyl)-1-(4-bromophenyl) methanimine (CD_3CN, 600 MHz, 298 K).

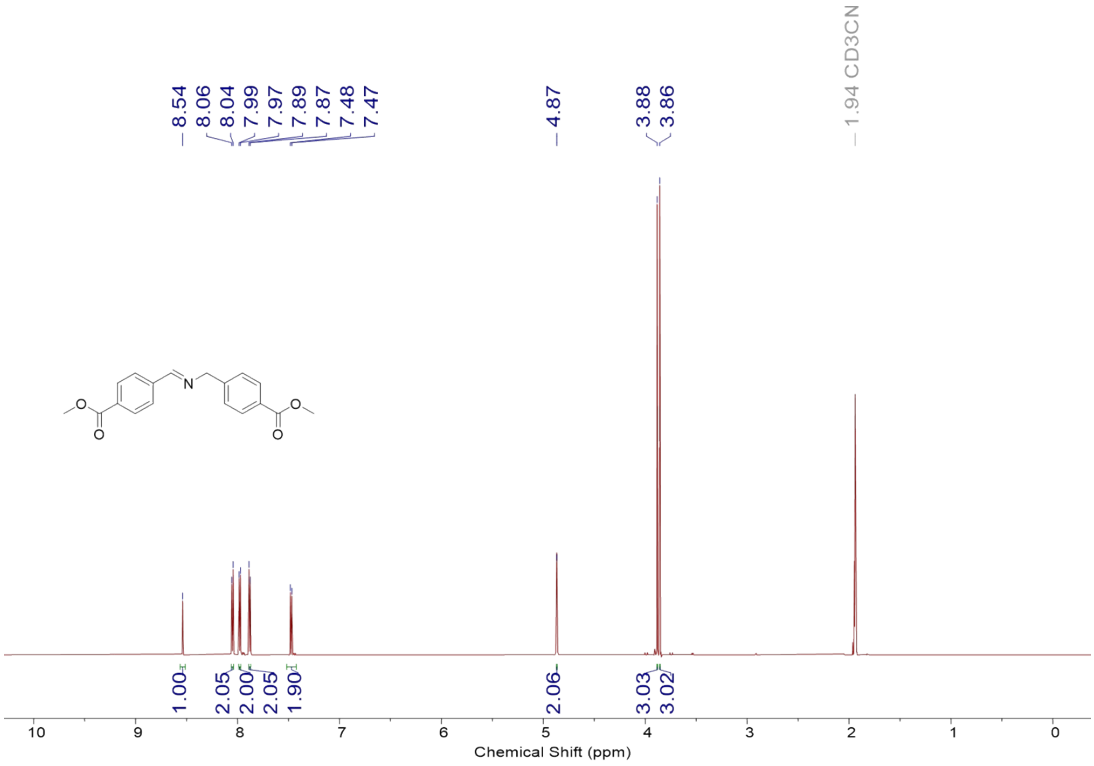

Figure S38. ^{1}H NMR spectra of *N*-(4-methoxycarbonylbenzyl)-N-(4-methoxycarbonylbenzylidene) amine (CD_3CN, 600 MHz, 298 K).

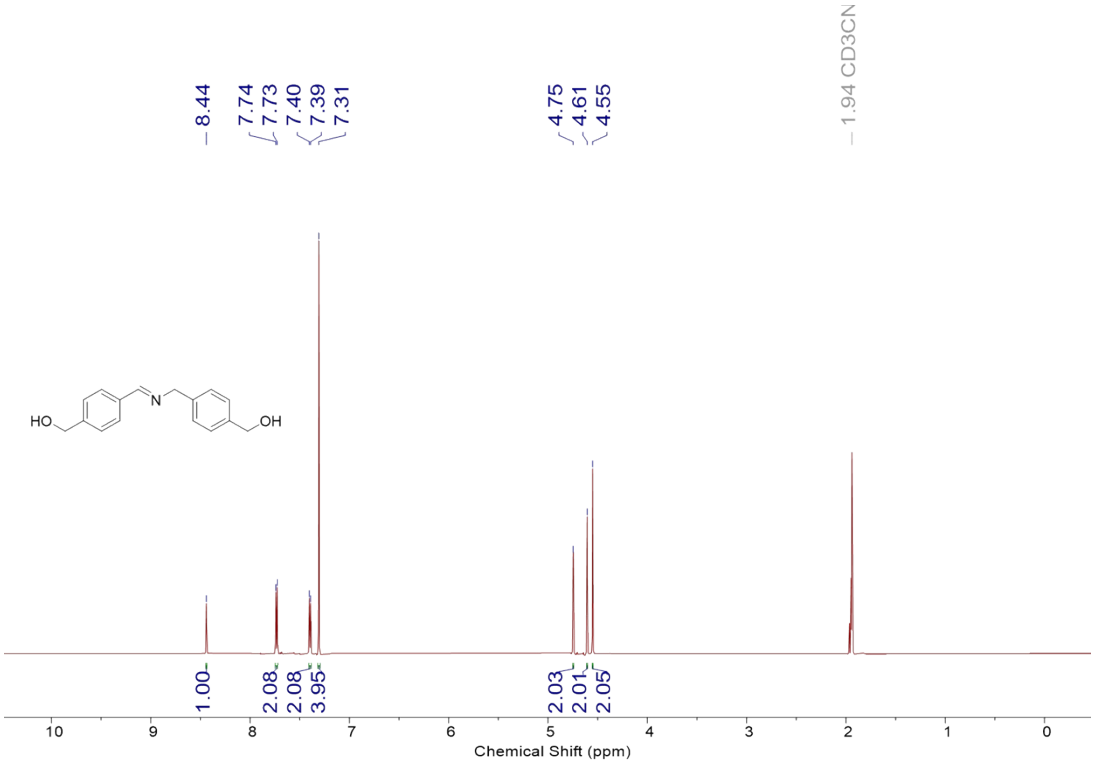

Figure S39. ^{1}H NMR spectra of (4-(((4-(hydroxymethyl)benzyl)imino)methyl)phenyl)methanol (CD_3CN, 600 MHz, 298 K).

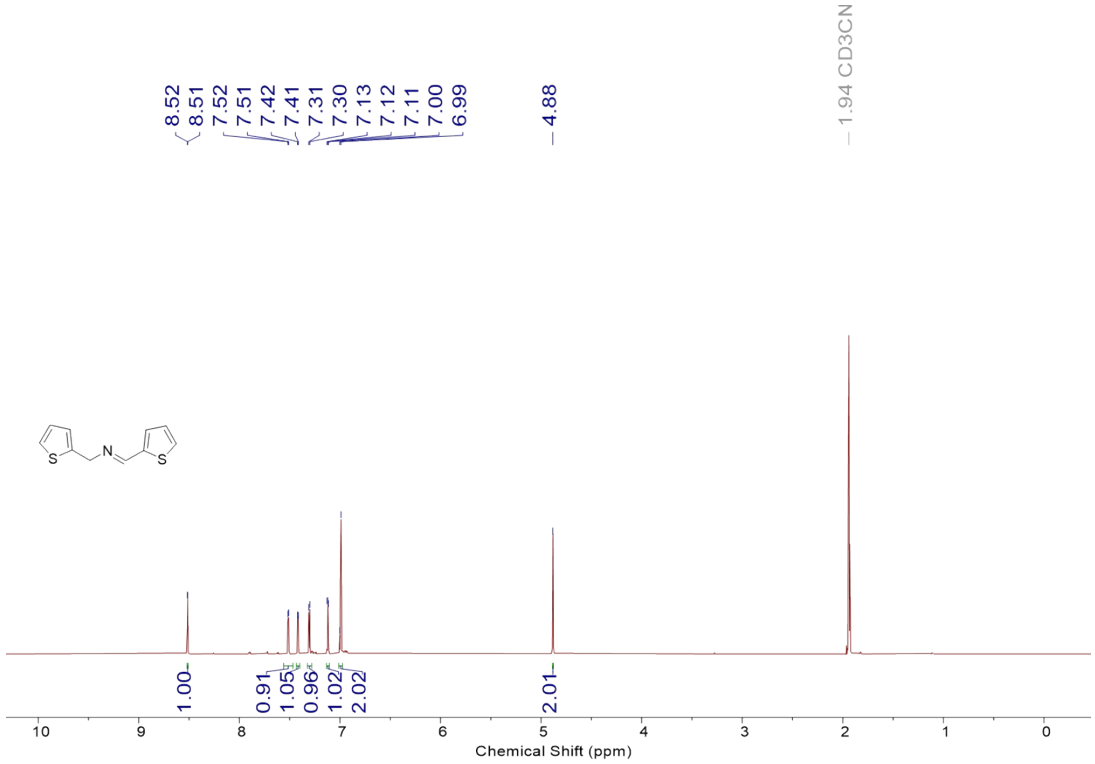

Figure S40. ^{1}H NMR spectra of *N*-(2-thienylmethylidene)-2-thienylmethylamine (CD_3CN, 600 MHz, 298 K).

Reference

1. Becke, A. D., Perspective: Fifty years of density-functional theory in chemical physics. *J. Chem. Phys.* **2014**, *140* (18), 18A301.

2. Adamo, C.; Jacquemin, D., The calculations of excited-state properties with Time-Dependent Density Functional Theory. *Chem. Soc. Rev.* **2013**, *42* (3), 845-856.

3. Gaussian 09, Revision D.01, M. J. Frisch, G. W. Trucks, H. B. Schlegel, G. E. Scuseria, M. A. Robb, J. R. Cheeseman, G. Scalmani, V. Barone, B. Mennucci, G. A. Petersson, H. Nakatsuji, M. Caricato, X. Li, H. P. Hratchian, A. F. Izmaylov, J. Bloino, G. Zheng, J. L. Sonnenberg, M. Hada, M. Ehara, K. Toyota, R. Fukuda, J. Hasegawa, M. Ishida, T. Nakajima, Y. Honda, O. Kitao, H. Nakai, T. Vreven, J. A. Montgomery, Jr., J. E. Peralta, F. Ogliaro, M. Bearpark, J. J. Heyd, E. Brothers, K. N. Kudin, V. N. Staroverov, T. Keith, R. Kobayashi, J. Normand, K. Raghavachari, A. Rendell, J. C. Burant, S. S. Iyengar, J. Tomasi, M. Cossi, N. Rega, J. M. Millam, M. Klene, J. E. Knox, J. B. Cross, V. Bakken, C. Adamo, J. Jaramillo, R. Gomperts, R. E. Stratmann, O. Yazyev, A. J. Austin, R. Cammi, C. Pomelli, J. W. Ochterski, R. L. Martin, K. Morokuma, V. G. Zakrzewski, G. A. Voth, P. Salvador, J. J. Dannenberg, S. Dapprich, A. D. Daniels, O. Farkas, J. B. Foresman, J. V. Ortiz, J. Cioslowski, and D. J. Fox, Gaussian, Inc., Wallingford CT, **2013**.

4. Stephens, P. J.; Devlin, F. J.; Chabalowski, C. F.; Frisch, M. J., Ab Initio Calculation of Vibrational Absorption and Circular Dichroism Spectra Using Density Functional Force Fields. *J. Phys. Chem.* **1994**, 98 (45), 11623-11627.

5. Binkley, J. S.; Pople, J. A.; Hehre, W. J., Self-consistent molecular orbital methods. 21. Small split-valence basis sets for first-row elements. *J. Am. Chem. Soc.* **1980**, 102 (3), 939-947.

6. Asselin, P.; Schlachter, A.; Fortin, D.; Karsenti, P.-L.; Harvey, P. D., Structural Influence on Exciton Migration and Singlet Oxygen Photosensitization in Porphyrinic Metal–Organic Coordination Networks. *Chem. Mater.* **2022**, 34 (16), 7242-7255.